

Distinct moiré trions in a twisted semiconductor homobilayer

Zhida Liu^{1,†}, Haonan Wang^{3,†}, Xiaohui Liu^{1,2}, Yue Ni¹, Frank Gao^{1,2}, Saba Arash^{1,2}, Dong Seob Kim¹, Xiangcheng Liu¹, Yongxin Zeng^{1,2}, Jiamin Quan¹, Di Huang¹, Kenji Watanabe⁴, Takashi Taniguchi⁵, Edoardo Baldini^{1,2}, Allan H. MacDonald^{1,2}, Chih-Kang Shih^{1,2}, Li Yang³, and Xiaoqin Li^{1,2*}

¹*Department of Physics and Center for Complex Quantum Systems, The University of Texas at Austin, Austin, Texas, 78712, USA.*

²*Center for Dynamics and Control of Materials and Texas Materials Institute, The University of Texas at Austin, Austin, Texas, 78712, USA.*

³*Department of Physics, Washington University in St Louis, St. Louis, MO, 63136, USA.*

⁴*Research Center for Electronic and Optical Materials, National Institute for Materials Science, 1-1 Namiki, Tsukuba 305-0044, Japan.*

⁵*Research Center for Materials Nanoarchitectonics, National Institute for Materials Science, 1-1 Namiki, Tsukuba 305-0044, Japan.*

† *These authors contributed equally.*

*Corresponding author: elaineli@physics.utexas.edu

July 25, 2024

Many fascinating properties discovered in graphene and transition metal dichalcogenide (TMD) moiré superlattices originate from flat bands and enhanced many-body effects. Here, we discover new many-electron excited states in TMD homobilayers. As optical resonances evolve with twist angle and doping in MoSe₂ bilayers, a unique type of “charge-transfer” trions is observed when gradual changes in atomic alignment between the layers occur. In real space, the optically excited electron-hole pair mostly resides in a different site from the doped hole in a moiré supercell. In momentum space, the electron-hole pair forms in the single-particle-band *K*-valley, while the hole occupies the Γ -valley. The rich internal structure of this trion resonance arises from the ultra-flatness of the first valence band and the distinct influence of moiré potential modulation on holes and excitons. Our findings open new routes to realizing photon-spin transduction or implementing moiré quantum simulators with independently tunable fermion and boson densities.

Semiconductor moiré superlattices formed by stacking two atomically thin layers have been established as a versatile platform to realize correlated electronic phases¹⁻⁴ and novel optical properties⁵⁻⁷. A variety of exciton resonances including intra-, interlayer, and hybrid excitons dominate the optical spectra of TMD bilayers. The resonant energy, dynamics, and nonlinear response of various excitonic resonances⁸⁻¹² are controllable by the twist angle between the layers¹³⁻¹⁵. When doping is introduced, correlated phases such as Wigner crystals and correlated insulator states have been observed in twisted TMD bilayers (e.g., WS₂/WSe₂). Early reports are often based on abrupt changes in exciton energy or photoluminescence intensity at fractional filling of moiré supercells^{16,17} although the underlying mechanism for such changes remains unclear. Doped moiré systems are considered a promising platform for quantum simulators that bridge naturally occurring materials with 0.1 nm unit cell and cold atom systems with 500 nm unit cells¹⁸.

Despite a rapidly growing number of studies devoted to optical properties of neutral or doped TMD moiré systems, the microscopic picture of moiré excitons remains elusive. The challenges mainly originate from the limited spatial resolution of optical experiments and the difficulty of performing first-principle calculations of many-body states in these complex structures. Previous reports relied on models that treated excitons as composite particles moving in a smooth moiré potential, a picture that is valid for large supercells^{19,20}. Because the conduction and valence band extrema may occur at different locations within a supercell²¹⁻²³, it is conceivable that many-body states with more complex internal structure may emerge²⁴. A notable example is a new type of “charge-transfer” exciton where the electron and hole reside in different locations within a supercell. Indeed, charge-transfer excitons have been recently identified in WSe₂/WS₂ bilayers by comparing first-principles calculations with measured optical spectra as a function of doping and magnetic field²⁵ and in a WS₂ bilayer by photocurrent experiments with atomic resolution²⁶.

Here, we investigate optical resonances in several MoSe₂ bilayers near *H*-stacking (i.e., $\theta = 60^\circ, 59.6^\circ, 59.2^\circ$ and 57.5°). Ultra-flat bands have been predicted in these homobilayers^{27,28} and the twist angle can be controlled with an accuracy better than 0.1° ²⁹, allowing us to investigate the influence of lattice reconstructions with known supercell sizes. By measuring the optical reflectivity spectra of several MoSe₂ bilayers as a function of doping, we discover a new type of positively charged trion, namely charge-transfer trions with a reduced binding energy ($\Delta_2 \sim 12$ meV). While tightly-bound trions ($\Delta_1 \sim 30$ meV) are observed in all three bilayers, the charge-transfer trions are only observed in the 57.5° bilayer with gradual atomic alignment changes between the two layers. First-principles calculations suggest that doped holes occupy a flat moiré band and are localized at

a particular site within the supercells. Optically excited electron-hole pairs may occupy either the same or a different location from the extra hole within the supercell, leading to the two different trion species. In contrast, charge-transfer trions are absent in the 59.6° and 59.2° bilayer because lattice reconstruction leads to commensurate domains^{30–32}. Our study reveals the complexity of new many-body states that emerge from the flat bands and different moiré modulation on electron-hole pairs and doped holes. Unlike interlayer moiré trions^{33–36}, the new trion resonance features strong oscillator strength, thus offering new opportunities to optically control an array of localized hole spins for quantum simulation and information processing analogous to those in conventional quantum dots^{37,38}.

Natural and twisted MoSe₂ bilayers encapsulated between hBN layers are incorporated in dual-gate devices (Fig. 1a and Extended Fig. 2), allowing us to tune the doping level and an out-of-plane electric field independently. All data presented in this paper are taken at zero electric field and a temperature of ~ 4.7 K unless stated otherwise. The details of the sample preparation and optical measurements can be found in the Methods section. In natural MoSe₂ bilayers ($\theta = 60^\circ$), the energetically favorable stacking is the AA' stacking where the centers of the hexagons in two layers coincide, and the Mo atoms in the top layer are vertically aligned with the Se atoms in the bottom layer. For a moderate twist angle (i.e., 57.5°), there is a systematic and gradual atomic alignment variation between the two layers as illustrated in Fig. 1b. In addition to the AA' stacking, two other high-symmetry stackings $A'B$ and AB' retain the three-fold rotational symmetry. At the $A'B$ (AB') points, the Se (Mo) atoms in the two layers are vertically aligned.

In moiré systems with a small twist angle from the commensurate H - and R -stacking, lattice

reconstructions driven by the competition between interlayer coupling and intrinsic strain can be described in three regimes^{31,39}. In the fully relaxed regime, lattices in both layers are slightly distorted to form large domains of low-energy stacking separated by sharp domain walls of high-energy stacking²³. As the twist angle increases to enter the transition regime, gradual atomic alignment variations appear. Experimentally, far-field spontaneous Raman scattering provides a valuable diagnostic tool for lattice reconstructions³¹. We compare the high-resolution Raman spectra from three MoSe₂ bilayers, as depicted in Fig. 1c. In the low-frequency range, only one shear (S) mode is observed in natural bilayers ($\theta = 60^\circ$) and fully relaxed kagome-like lattices ($\theta = 59.2^\circ$ and 59.6°)²³. In contrast, the emergence of the layer breathing (LB) mode in the $\theta = 57.5^\circ$ bilayer suggests that gradual atomic variations occur in this sample⁴⁰. For the rest of this paper, our main focus is the 57.5° twisted bilayer with ~ 8 nm supercells, corresponding to a supercell density of $2 \times 10^{12} \text{cm}^{-2}$. We compare the spectra taken on the natural bilayer, fully relaxed 59.2° and the 57.5° bilayers. Optical spectra and low frequency Raman from the fully relaxed 59.6° bilayer are qualitatively similar to those in the 59.2° bilayer, as shown in Extended Fig. 2.

We then measure the optical reflectivity spectra from the natural bilayer, 59.2° and 57.5° twisted bilayers. The two-dimensional (2D) contours as a function of doping density and energy are shown in Fig. 2 a,c,e, respectively. When electron doping increases in the natural bilayer, the A exciton (X_A) evolves into two branches, exhibiting either a continuous red-shift (E_1) or a blue-shift. These features are often attributed to the formation of attractive and repulsive Fermi polarons^{41,42}. On the hole doping side, in addition to a blue-shift resonance from the A exciton, a

positive trion (H_1) is observed at low doping densities. Trions are three-particle bound states with a certain binding energy, a concept that holds at low doping density. In the case of H_1 in the natural and 59.2° twisted bilayer, the binding energy is approximately 29 meV⁴³. In the 57.5° twisted bilayer, a new trion resonance H_2 with a smaller binding energy of ~ 12 meV appears in addition to the negative trion E_1 and positive trion H_1 found in other bilayers. Multiple horizontal linecuts taken at several doping densities in all three bilayers are displayed in Fig. 2b,d,f, respectively. The peak energies of both trions (H_1 and H_2) are indicated by circles, following fitting with multiple Lorentzian functions (Details are in Method and examples of fitted spectra are in Extended Fig. 3).

To interpret the measured optical spectra, we first perform first-principles calculations and examine the electronic band structure with many-body effects. We perform single-shot G_0W_0 calculations of the electronic structure of the natural MoSe₂ bilayer (e.g., local bands at the AA' stacking site)⁴⁴. As expected, the electronic self-energy significantly increases the density functional theory (DFT) band gap from 1.14 eV to 1.75 eV (see details in the Supplementary Materials). More importantly, the quasiparticle conduction band minimum (CBM) experiences a shift from the K point to the Q point, while the valence band maximum (VBM) remains at the Γ point, as shown in Fig. 3a. Thus, doped holes (electrons) are mainly located at the Γ (Q) point in the momentum space, as illustrated in Fig. 3b. Within this picture, a doped hole at the Γ point couples with an electron-hole pair from the K - K transition to form an optically bright three-particle bound state.

To confirm the distribution of dopants in momentum space, we conduct helicity-resolved magneto-optical reflectivity measurements at 2.5 T. Several spectra at various electron and hole doping densities are displayed in Fig. 3c and 3d. The electron-doped spectra reveal a significant

Zeeman splitting associated with spin-polarized electrons at the Q valleys⁴⁵. Fitting the spectra with Lorentz functions and using the simple relation $\Delta E = g\mu_B B$, where ΔE is the energy difference between σ^- and σ^+ excitations, we extract a g-factor of 20 ± 1.4 at $1.1 \times 10^{12} \text{ cm}^{-1}$. In contrast, helicity-resolved reflectivity measurements at several hole doping densities taken at 2.5 T reveal minimal spectral shift for both H_1 and H_2 . This distinct magnetic field dependence is attributed to doped holes at the Γ valley with spin degeneracy. Another piece of evidence supporting the distribution of doped holes at the Γ valley is found by examining the red-shift of H_1 and H_2 at high doping density (data shown in Extended Fig. 4). Both spectroscopic features for Γ valley holes are consistent with a previous study on $\text{MoSe}_2/\text{WSe}_2$ heterostructures⁴⁶.

We then calculate the single-particle bands of twisted bilayers in the single-particle picture. Subjected to three-fold rotational symmetry of a bilayer, the quasiparticle moiré potential can be approximated through a first-order Fourier expansion,

$$\Delta(\mathbf{r}) = V_0 + V_1 \sum_{j=1,3,5} \cos(\mathbf{G}_j \cdot \mathbf{r} + \psi), \quad (1)$$

where the summation runs over the three-nearest neighbor reciprocal lattices, and \mathbf{G} denotes the reciprocal lattice vector of the moiré superlattice. The equation of motion of doped carriers is determined by the quasiparticle moiré Hamiltonian,

$$\mathcal{H} = \frac{\hbar^2 \mathbf{Q}^2}{2m^*} + \Delta(\mathbf{r}), \quad (2)$$

where the first term denotes the kinetic energy with m^* representing the quasiparticle effective mass. All parameters in Eq. (2) can be determined from first-principles GW calculations at three high-symmetry stacking (AA' , $A'B$, and AB'). Our calculations reveal that the atomic reconstruction around AA' and $A'B$ stackings is negligible at 57.5° , despite being significant at 59.2° and

in other moiré systems^{23,25} (see details in Extended Fig. 6 and in Supplementary Materials). The obtained moiré band structure at 57.5° is presented in Fig. 3e. The emergent flat valence moiré bands are consistent with previous computational studies^{27,28}. The contour and intersection plots of the charge density of the highest valence band are presented in Figs. 4a-b, indicating that doped holes predominantly occupy the AA' region.

Next, we calculate the two-particle excitation (exciton) spectrum in a twisted bilayer. The exciton Bohr radius is significantly smaller than the moiré period at the 57.5° . Thus, we can treat the lowest energy exciton as a composite particle moving within a slowly varying exciton moiré potential. We first solve the Bethe-Salpeter Equation (BSE)⁴⁷ at three high-symmetry stacking sites (AA' , $A'B$, and AB') to obtain exciton energies and dipole oscillator strengths (details are in the Supplementary Materials). Taking into account the exciton energy, the exciton moiré potential is solved approximately using Eq. (1). The final step in finding the exciton spatial distribution is to solve Eq. (2) with exciton moiré potential and effective mass. Two excitons (X^1 and X^2) residing at the potential minimal of AA' and AB' (Fig. 4c-d) are nearly degenerate, with a small energy difference of 2 meV. These two exciton states are spectrally unresolved in experiments, i.e., only one resonance (X_A) is observed in the intrinsic (undoped) regime in the measured spectra Fig. 2b. Their distinct spatial distribution is manifested in the measured spectra when hole doping is introduced. Because doped holes always reside on the AA' sites, two types of trions (H_1 and H_2) form as illustrated in Fig. 4e. In the case of the H_1 resonance, the exciton X^1 significantly overlaps with the doped hole, resulting in strong exciton-hole binding energy and a tightly bound trion. In the contrary, because of the spatial separation between the doped hole and exciton X^2 ,

the charge-transfer H_2 exhibits a smaller binding energy.

We discuss our findings in the context of prior studies. Recent experiments have combined optical excitation with powerful techniques with high spatial and/or momentum resolution (e.g., time-resolved momentum microscopy⁴⁸ and transmission electron microscopy and spectroscopy⁴⁹) and brought new insights into exciton physics in TMD moiré superlattices. Our proposed microscopic pictures for two types of trions with distinct internal structures are consistent with these recent experiments imaging localized excitons or holes and serve as a valuable guidance to future experiments. For charge transfer excitons in twisted WS_2 bilayers, the spatial separation of electron and hole within a supercell has been directly visualized using scanning tunneling microscopy with atomic resolution^{22,50}. In the case of WSe_2/WS_2 bilayers, the doped holes forming a regular electron crystal, (i.e., a Wigner crystal state) at a certain fractional filling have also been directly imaged⁵¹. The real space localization is consistent with the flat valence band. In WSe_2/WS_2 bilayers, where both Wannier-type and charge-transfer excitons have been identified²⁵. The energy shift between the Wannier and charge-transfer excitons is more than 100 meV, and the electron-hole separation of the charge-transfer exciton is estimated to be ~ 5 nm. As hole doping is introduced in the WSe_2/WS_2 bilayers, a continuous energy shift was observed and attributed to the Coulomb interactions between doped carriers and moiré excitons. In the case of twisted MoSe_2 bilayers studied here, the optically created electron and hole reside in the same location within the supercell and bind to form Wannier-type excitons. They occupy two nearly degenerate sites within the supercell. As doped holes are introduced, they localize at the AA' site as a result of the ultra-flat valence band. Two types of bound trion resonances are identified depending on

whether the Wannier excitons and holes occupy the same site (tightly bound trions) as or different sites (charge-transfer trions). For the charge-transfer trion in the 57.5° MoSe₂ bilayer, the hole is separated by the Wannier intralayer exciton by approximately 2.5 nm laterally.

In conclusion, we investigated the influence of the ultra-flat valence band and the different moiré modulation experienced by electrically doped holes and optically created electron-hole pairs in twisted MoSe₂ bilayers. Two types of positive trions form at low hole doping density in twisted bilayers only if the lattice is not fully relaxed. The newly identified charge-transfer trions is at lower energy than excitons. Moiré trions feature complex quantum indices including spin, momentum, and valley, and thus, they offer new opportunities of optical control of spins and valley pseudo-spins as well as engineering excitonic phases or quantum simulators where the density of fermions (i.e., doped holes and trions) and bosons (i.e., excitons) can be independently controlled¹⁶.

Methods

Device fabrication and optical measurements: MoSe₂ monolayers, bilayers, and hBN encapsulated layers were exfoliated from high-quality bulk crystals. As illustrated in Fig. 1a and Extended Fig. 1, the dual gate devices consisted of a few-layer graphite top gate (TG) and a metallic back gate (BG), which enabled us to tune the carrier density and electric field independently. We used the tear-and-stack method to control the twist angle with an accuracy better than 0.1° . Optical measurements were carried out in a home-built confocal microscope using an objective with a numerical aperture of 0.5 at 4.7 K in a closed-cycle cryostat. To obtain the reflectance spectra, a halogen lamp was used as the light source. The charge densities n were calculated using a parallel capacitor model, $n = \frac{\epsilon_r \epsilon_0 (V_t - V_{t0}) / d_{top} + \epsilon_r \epsilon_0 (V_b - V_{b0}) / d_{bottom}}{e}$, where ϵ_r is the relative permittivity of

hBN chosen 4.2 here ⁴ and V_{t0} and V_{b0} are the top and bottom gate voltages at which the $1S$ exciton signal starts to change under electron and hole doping. The thickness of the top and bottom hBN layers (i.e., d_{top} and d_{bottom}) in 57.5° twisted bilayer are 25 nm and 35 nm respectively, according to AFM measurements.

Reflectivity spectra fitting: We define the differential reflectance as $\Delta R/R_0$ where R_0 is the background signal measured in a region without the MoSe₂ flake. The reflectance signal is modeled as a multi-Lorentzian lineshape with a phase shift α that depends on the energy and gate voltage ³. For each resonance, $\Delta R/R_0 = \frac{A \cos(\alpha) \gamma^2 / 2}{(E-E_0)^2 + \gamma^2 / 4} + \frac{A \sin(\alpha) \gamma (E-E_0)}{(E-E_0)^2 + \gamma^2 / 4} + c$, where A is the amplitude, E_0 is peak energy, γ is linewidth and c is offset constant.

Computational methods: First-principles calculations based on DFT are performed within the general gradient approximate (GGA) using the Perdew-Burke-Ernzerhof (PBE) exchange-correlation functional as implemented in the Quantum ESPRESSO package ⁵². The vdW interactions were included via the Grimme-D2 scheme ⁵³. The plane-wave energy cutoff is 60 Ry. The vacuum distance between adjacent layers was set to be 20 Å. An $18 \times 18 \times 1$ k-grid was sampled in the reciprocal space. The quasiparticle energies were calculated by the single-shot G_0W_0 approximation using the general plasmon pole model ⁴⁴ including the slab Coulomb truncation. 354 unoccupied bands were used to calculate the dielectric function. The lowest-energy exciton energy was calculated from GW plus Bethe-Salpeter calculations ⁴⁷. The energy impact from the spin-orbit coupling was included using the DFT corrections to the GW quasiparticle and exciton energies.

References

1. Wang, L. et al. Correlated electronic phases in twisted bilayer transition metal dichalcogenides. Nature Materials **19**, 861–866 (2020).
2. Tang, Y. et al. Simulation of Hubbard model physics in WSe₂/WS₂ moiré superlattices. Nature **579**, 353–358 (2020).
3. Shimazaki, Y. et al. Strongly correlated electrons and hybrid excitons in a moiré heterostructure. Nature **580**, 472–477 (2020).
4. Regan, E. C. et al. Mott and generalized Wigner crystal states in WSe₂/WS₂ moiré superlattices. Nature **579**, 359–363 (2020).
5. Regan, E. C. et al. Emerging exciton physics in transition metal dichalcogenide heterobilayers. Nature Reviews Materials **7**, 778–795 (2022).
6. Huang, D., Choi, J., Shih, C.-K. & Li, X. Excitons in semiconductor moiré superlattices. Nature Nanotechnology **17**, 227–238 (2022).
7. Andersen, T. I. et al. Excitons in a reconstructed moiré potential in twisted WSe₂/WSe₂ homobilayers. Nature Materials **20**, 480–487 (2021).
8. Tran, K. et al. Evidence for moiré excitons in Van der Waals heterostructures. Nature **567**, 71–75 (2019).
9. Seyler, K. L. et al. Signatures of moiré-trapped valley excitons in MoSe₂/WSe₂ heterobilayers. Nature **567**, 66–70 (2019).

10. Jin, C. et al. Observation of moiré excitons in WSe_2/WS_2 heterostructure superlattices. Nature **567**, 76–80 (2019).
11. Alexeev, E. M. et al. Resonantly hybridized excitons in moiré superlattices in Van der Waals heterostructures. Nature **567**, 81–86 (2019).
12. Zhang, N. et al. Moiré intralayer excitons in a $\text{MoSe}_2/\text{MoS}_2$ heterostructure. Nano letters **18**, 7651–7657 (2018).
13. Merkl, P. et al. Twist-tailoring Coulomb correlations in Van der Waals homobilayers. Nature Communications **11**, 2167 (2020).
14. Choi, J. et al. Twist angle-dependent interlayer exciton lifetimes in Van der Waals heterostructures. Physical Review Letters **126**, 047401 (2021).
15. Zhang, L. et al. Twist-angle dependence of moiré excitons in $\text{WS}_2/\text{MoSe}_2$ heterobilayers. Nature Communications **11**, 5888 (2020).
16. Xiong, R. et al. Correlated insulator of excitons in WSe_2/WS_2 moiré superlattices. Science eadd5574 (2023).
17. Xu, Y. et al. Correlated insulating states at fractional fillings of moiré superlattices. Nature **587**, 214–218 (2020).
18. Kennes, D. M. et al. Moiré heterostructures as a condensed-matter quantum simulator. Nature Physics **17**, 155–163 (2021).

19. Wu, F., Lovorn, T. & MacDonald, A. H. Topological exciton bands in moiré heterojunctions. Physical Review Letters **118**, 147401 (2017).
20. Brem, S., Linderalv, C., Erhart, P. & Malic, E. Tunable phases of moiré excitons in Van der Waals heterostructures. Nano Letters **20**, 8534–8540 (2020).
21. Zhang, Z. et al. Flat bands in twisted bilayer transition metal dichalcogenides. Nature Physics **16**, 1093–1096 (2020).
22. Li, H. et al. Imaging local discharge cascades for correlated electrons in WS_2/WSe_2 moiré superlattices. Nature Physics **17**, 1114–1119 (2021).
23. Weston, A. et al. Atomic reconstruction in twisted bilayers of transition metal dichalcogenides. Nature Nanotechnology **15**, 592–597 (2020).
24. Zeng, Y. & MacDonald, A. H. Strong modulation limit of excitons and trions in moiré materials. Physical Review B **106**, 035115 (2022).
25. Naik, M. H. et al. Intralayer charge-transfer moiré excitons in Van der Waals superlattices. Nature **609**, 52–57 (2022).
26. Li, H. et al. Imaging moiré excited states with photocurrent tunnelling microscopy. Nature materials 1–6 (2024).
27. Naik, M. H., Kundu, S., Maity, I. & Jain, M. Origin and evolution of ultraflat bands in twisted bilayer transition metal dichalcogenides: Realization of triangular quantum dots. Physical Review B **102**, 075413 (2020).

28. Xian, L. et al. Realization of nearly dispersionless bands with strong orbital anisotropy from destructive interference in twisted bilayer MoS₂. Nature Communications **12**, 5644 (2021).
29. Kim, K. et al. Van der Waals heterostructures with high accuracy rotational alignment. Nano Letters **16**, 1989–1995 (2016).
30. Zhao, S. et al. Excitons in mesoscopically reconstructed moiré heterostructures. Nature nanotechnology **18**, 572–579 (2023).
31. Quan, J. et al. Phonon renormalization in reconstructed MoS₂ moiré superlattices. Nature Materials **20**, 1100–1105 (2021).
32. Sung, J. et al. Broken mirror symmetry in excitonic response of reconstructed domains in twisted MoSe₂/MoSe₂ bilayers. Nature Nanotechnology **15**, 750–754 (2020).
33. Wang, X. et al. Intercell moiré exciton complexes in electron lattices. Nature Materials 1–6 (2023).
34. Wang, X. et al. Moiré trions in MoSe₂/WSe₂ heterobilayers. Nature Nanotechnology **16**, 1208–1213 (2021).
35. Liu, E. et al. Signatures of moiré trions in WSe₂/MoSe₂ heterobilayers. Nature **594**, 46–50 (2021).
36. Brotons-Gisbert, M. et al. Moiré-trapped interlayer trions in a charge-tunable WSe₂/MoSe₂ heterobilayer. Physical Review X **11**, 031033 (2021).

37. Kroutvar, M. et al. Optically programmable electron spin memory using semiconductor quantum dots. Nature **432**, 81–84 (2004).
38. Gerardot, B. D. et al. Optical pumping of a single hole spin in a quantum dot. Nature **451**, 441–444 (2008).
39. Carr, S., Fang, S. & Kaxiras, E. Electronic-structure methods for twisted moiré layers. Nature Reviews Materials **5**, 748–763 (2020).
40. Puretzy, A. A. et al. Twisted MoSe₂ bilayers with variable local stacking and interlayer coupling revealed by low-frequency Raman spectroscopy. ACS Nano **10**, 2736–2744 (2016).
41. Efimkin, D. K., Laird, E. K., Levinsen, J., Parish, M. M. & MacDonald, A. H. Electron-exciton interactions in the exciton-polaron problem. Physical Review B **103**, 075417 (2021).
42. Sidler, M. et al. Fermi polaron-polaritons in charge-tunable atomically thin semiconductors. Nature Physics **13**, 255–261 (2017).
43. Gao, S., Liang, Y., Spataru, C. D. & Yang, L. Dynamical excitonic effects in doped two-dimensional semiconductors. Nano letters **16**, 5568–5573 (2016).
44. Hybertsen, M. S. & Louie, S. G. Electron correlation in semiconductors and insulators: Band gaps and quasiparticle energies. Physical Review B **34**, 5390–5413 (1986).
45. Förste, J. et al. Exciton g-factors in monolayer and bilayer WSe₂ from experiment and theory. Nature Communications **11**, 4539 (2020).

46. Campbell, A. J. et al. The interplay of field-tunable strongly correlated states in a multi-orbital moiré system. Nature Physics 1–8 (2024).
47. Rohlfing, M. & Louie, S. G. Electron-hole excitations and optical spectra from first principles. Physical Review B **62**, 4927–4944 (2000).
48. Karni, O. et al. Structure of the moiré exciton captured by imaging its electron and hole. Nature **603**, 247–252 (2022).
49. Susarla, S. et al. Hyperspectral imaging of exciton confinement within a moiré unit cell with a subnanometer electron probe. Science **378**, 1235–1239 (2022).
50. Li, H. et al. Imaging two-dimensional generalized Wigner crystals. Nature **597**, 650–654 (2021).
51. Li, H. et al. Wigner molecular crystals from multi-electron moiré artificial atoms. arXiv preprint arXiv:2312.07607 (2023).
52. Giannozzi, P. et al. Quantum espresso: a modular and open-source software project for quantum simulations of materials. Journal of Physics: Condensed matter **21**, 395502 (2009).
53. Grimme, S. Accurate description of Van der Waals complexes by density functional theory including empirical corrections. Journal of Computational Chemistry **25**, 1463–1473 (2004).

Data availability

Source data are provided with this paper. The data that support the plots within this paper and other findings of this study are available from the corresponding authors upon reasonable requests.

Acknowledgements

The experiments are primarily supported by the National Science Foundation via grant NSF ECCS-2130552 (Z. Liu and D. Kim). X. Li and Y. Ni gratefully acknowledge partial support from the Department of Energy, Office of Basic Energy Sciences under grant DE-SC0019398 for device fabrication and the Welch Foundation chair F-0014 for sample preparation. H.W. is supported by the National Science Foundation (NSF) grant No. DMR-2124934. The collaboration between UT-Austin (S. A.) and Washington University was enabled by NSF Designing Materials to Revolutionize and Engineer our Future (DMREF) program via grants DMR-2118806 and DMR-2118779. We acknowledge the partial support from the National Science Foundation through the Center for Dynamics and Control of Materials: an NSF MRSEC under Cooperative Agreement No. DMR-1720595, which has enabled to collaboration between Shih, MacDonald, Baldini, and Li and supported the user facility where part of the experiments were performed. The Major Research Instrumentation (MRI) program DMR-2019130 supported the Raman experiment facility. Work in the Baldini group at UT Austin was primarily supported by the Robert A. Welch Foundation under grant F-2092-20220331 (to F.Y.G. for data taking and analysis) and the United States Army Research Office (W911NF-23-1-0394) (to E.B. for experimental support and manuscript editing). K.W. and T.T. acknowledge support from the JSPS KAKENHI (Grant Numbers 20H00354, 21H05233 and 23H02052) and World Premier International Research Center Initiative (WPI), MEXT, Japan. The computing resource is provided by Purdue Anvil at the Rosen Center for Advanced Computing through allocation DMR100005 from the Advanced Cyberinfrastructure Coordination Ecosystem: Services Support (ACCESS) program, which is supported by

National Science Foundation grants 2138259, 2138286, 2138307, 2137603, and 2138296.

Author contributions

Z.L. and X.Li conceived the experiments. Z.L. fabricated the samples with assistance from Y.N., XH.Liu, XC.Liu, J.M.. Z.L. carried out optical experiments and analyzed data with assistance from F.G., S.A., D.H., H.W., D.S.K, CK.S.,E.B. and X.Li. K.W and T.T synthesized the hBN bulk crystals. A.H.M. and Y.Z. proposed the theoretical model. H.W. performed the first-principles calculations under the supervision of L.Y.. Z.L., H.W., L.Y., and X.Li. wrote the first draft of the manuscript. All authors contributed to discussions and provided input to the manuscript.

Competing interests

The authors declare no competing interests.

Figures

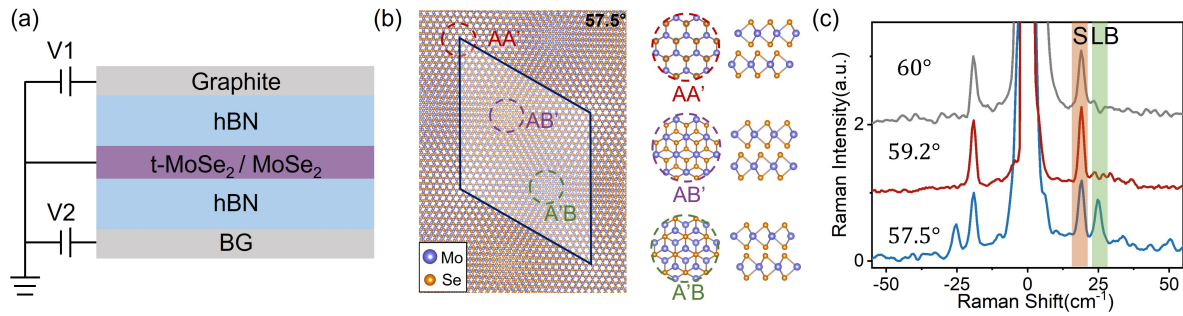


Figure 1: Schematics of the MoSe₂ bilayer device and local stacking at three high symmetry points. (a) Dual-gate device used to control the doping density in MoSe₂ bilayers. (b) Illustration of gradual variations of atomic alignment in twisted bilayers that are not fully relaxed structurally. Three high symmetry points are labelled as AA' (H_{Se}^{Mo}), AB' (H_{Mo}^{Mo}). The notation H refers to near- H stacking and the superscript (subscript) refers to atoms in the top (bottom) layer. (c) Raman spectra from three bilayers with θ of 60° (grey), 59.2° (red), and 57.5° (blue), respectively. A shear mode (S), indicated by the orange stripe, is present in all three bilayers while the layer breathing (LB) mode, indicated by the green stripe, is only observable in the $\theta = 57.5^\circ$ bilayer.

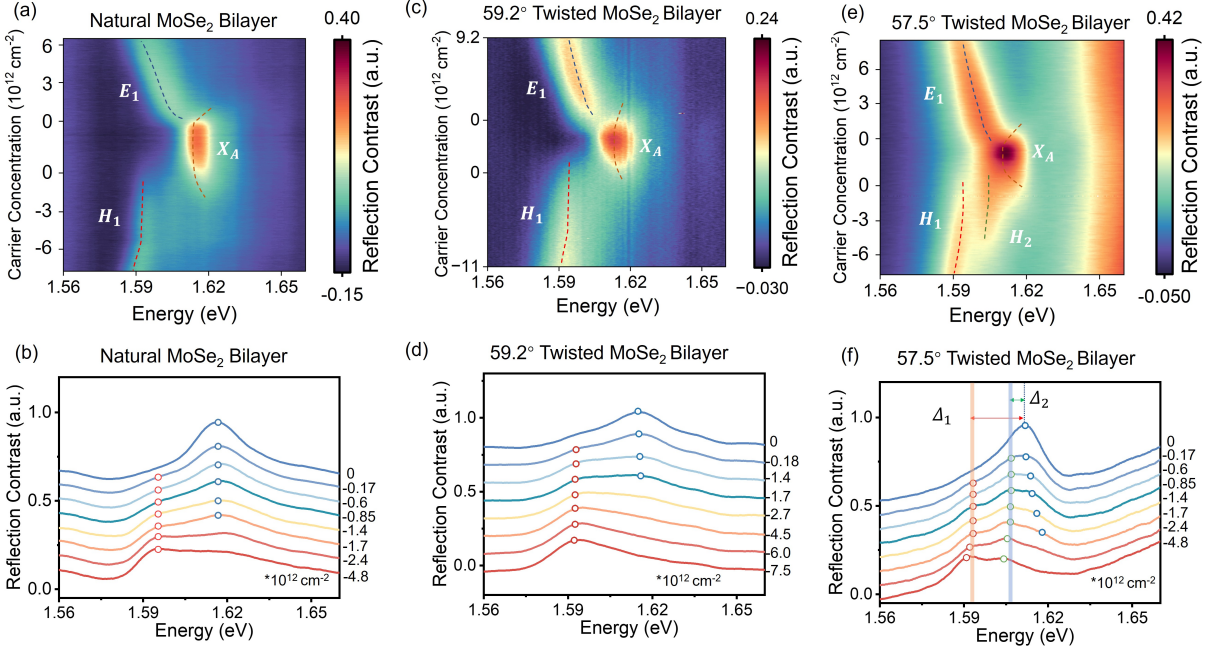


Figure 2: Doping dependent differential reflectivity in three different bilayers. Differential reflectivity spectra of (a) a natural bilayer, (c) a fully relaxed 59.2° , and (e) a 57.5° bilayer. In both (a) and (c), the A exciton resonance in the intrinsic regime evolves into two branches with electron doping. The lower energy E_1 resonance red-shifts with increasing electron doping. With hole doping, a bound state H_1 forms and only red-shifts beyond a certain hole doping density. In (e) a new trion resonance H_2 appears. Dashed lines serve as the guide-to-the-eye highlighting the energy shifts of different resonances. Linecuts of reflectivity spectra taken at several doping densities in (b) the natural bilayer, (d) the 59.2° , and (f) the 57.5° bilayer. Δ_1 (Δ_2) corresponds to the binding energy of H_1 (H_2).

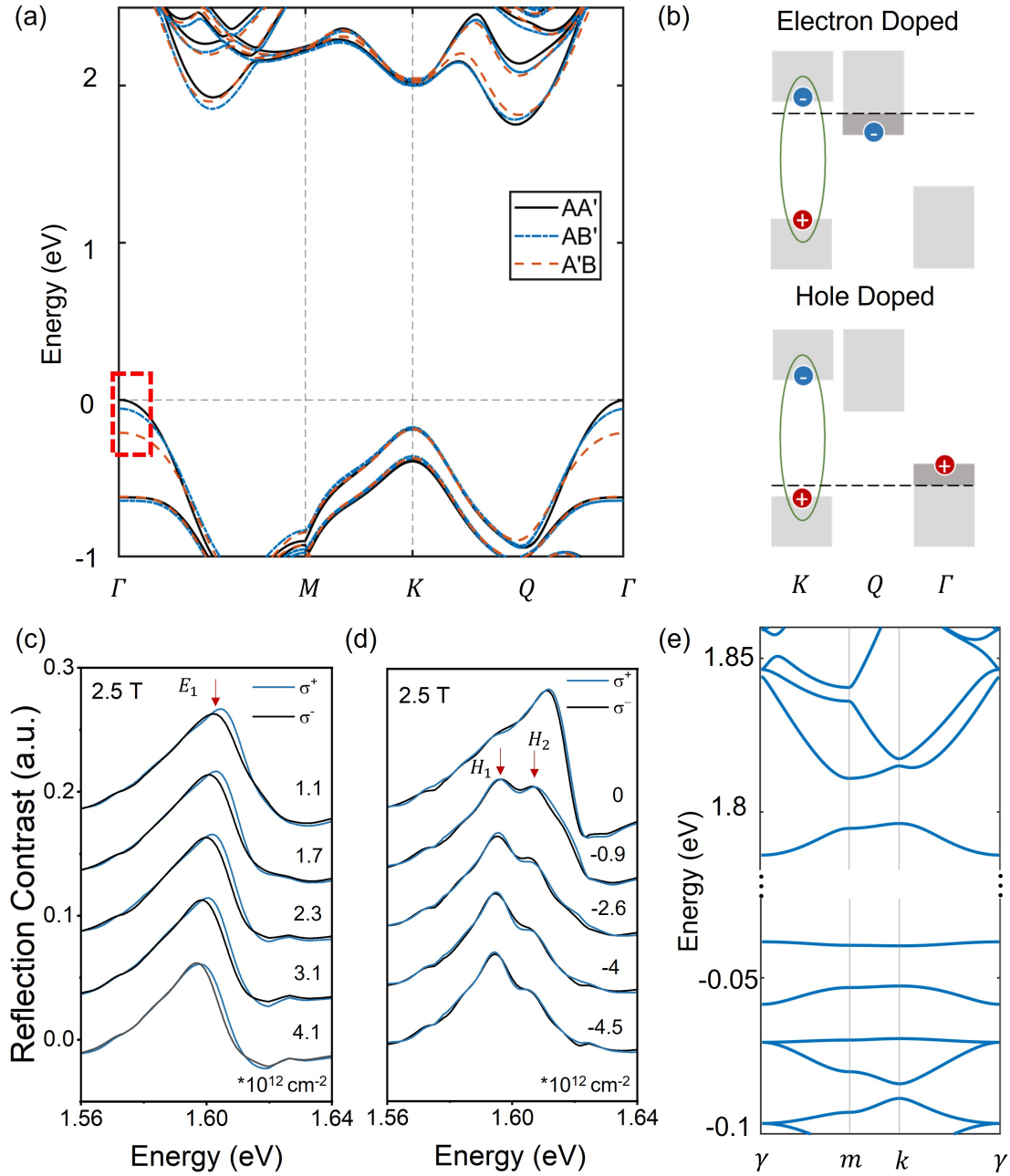


Figure 3: Band structure calculations and trion configurations in momentum space. (a) Electronic band structures calculated for three high-symmetry stacking configurations (AA', AB', A'B) of MoSe₂ bilayers. (b) Trion configurations in momentum space. The top panel shows that doped electrons reside at the Q valleys of the first CBM. The bottom panel shows that doped holes first occupy the Γ valleys at the first VBM. (c,d) Helicity-resolved reflectivity linecuts taken in the presence of 2.5 T magnetic field at several different (c) electron and (d) hole doping densities. (e) Moiré minibands of the 57.5° twisted bilayer displayed in the moiré Brillouin zone where VBM is at the γ point.

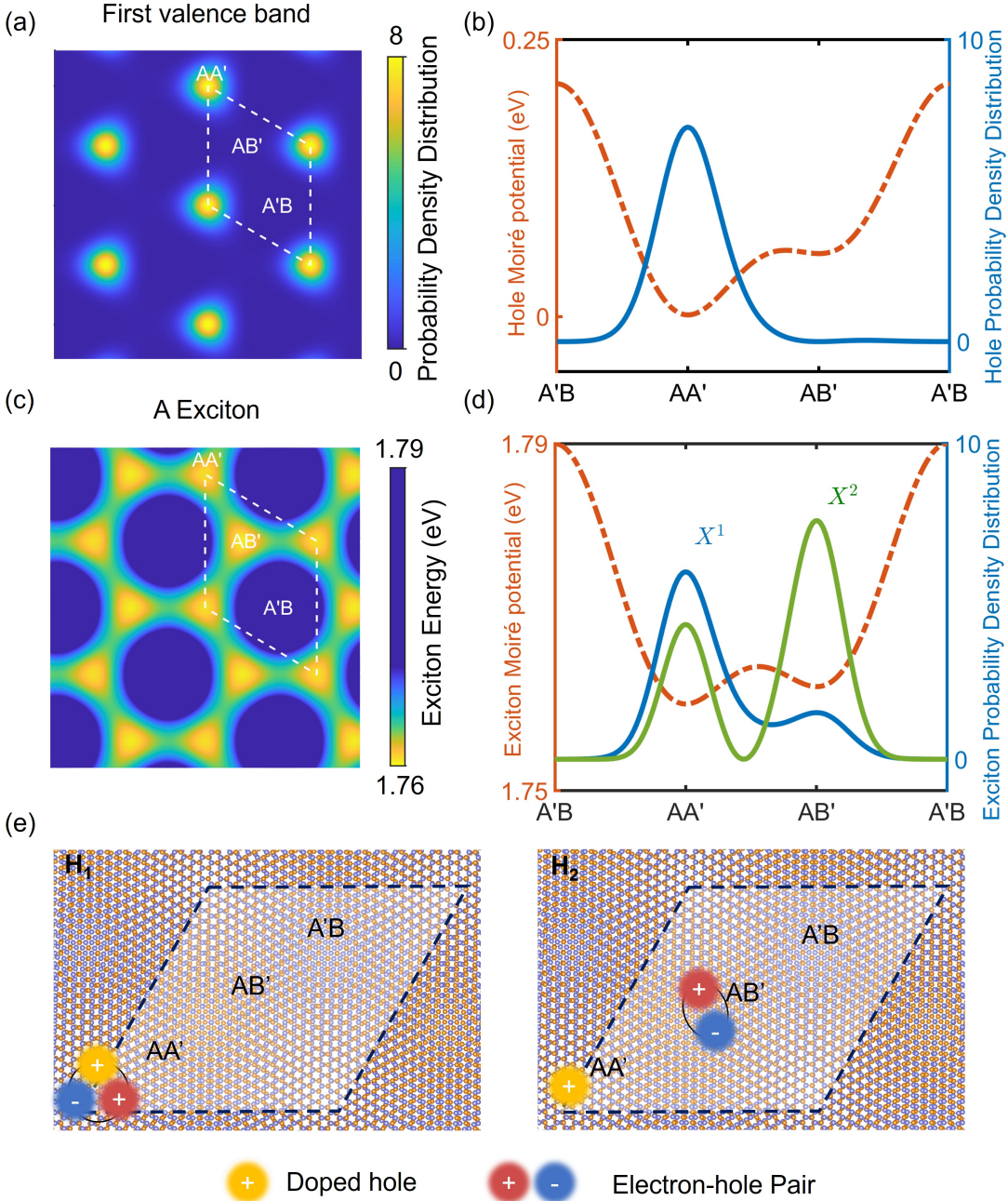
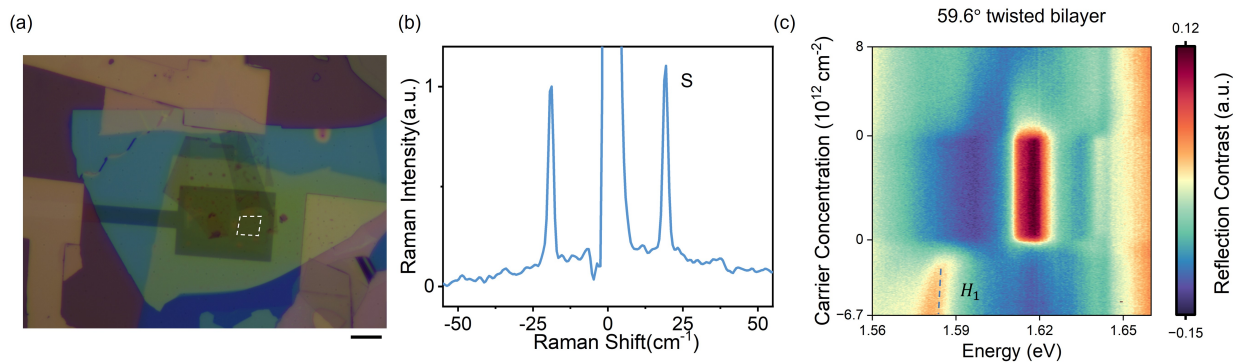


Figure 4: Spatial distributions of hole states, excitons, trions. (a) Probability density distribution of the first moiré valence band at the γ point. (b) Hole moiré potential (red dash-dotted line) and probability density (blue solid line) of the first moiré valence miniband along the high-symmetry stacking line. The doped holes are mainly localized at the AA' site. (c) Lowest exciton energy distributions where the exciton moiré potential only differs by ~ 2 meV between the AA' and AB' sites. (d) Exciton moiré potential (red dash-dotted line), probability density distribution of the lowest (blue solid line) and second lowest (green solid line) moiré exciton states along the high-symmetry stacking line. (e) Illustration of two types of positively charged trions where the extra hole is at the same (different) location as the electron-hole pair for H_1 (H_2).

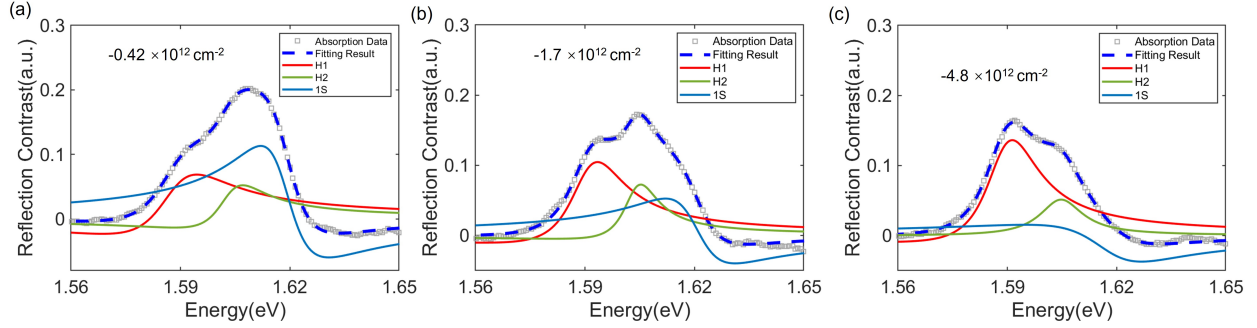
Extended Data



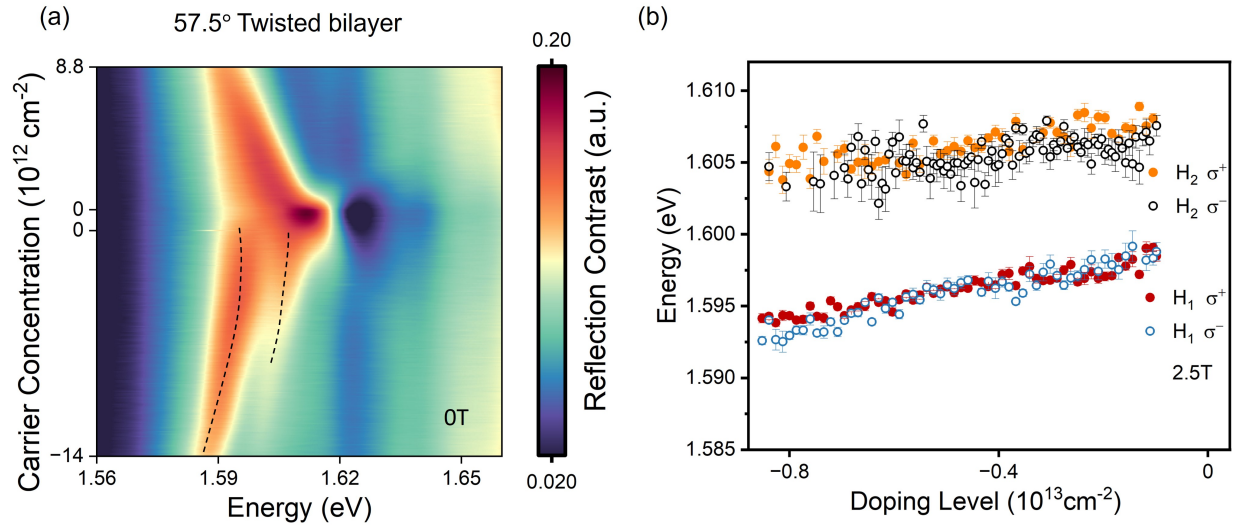
Extended Data Fig. 1: Images of samples in the main text. (a-c) Optical microscopy picture of the natural bilayer MoSe₂ (a), 57.5° twisted bilayer (b) and 59.2° bilayer (c). The white dashed line shows the twisted bilayer region. The scale bar is 10 μm .



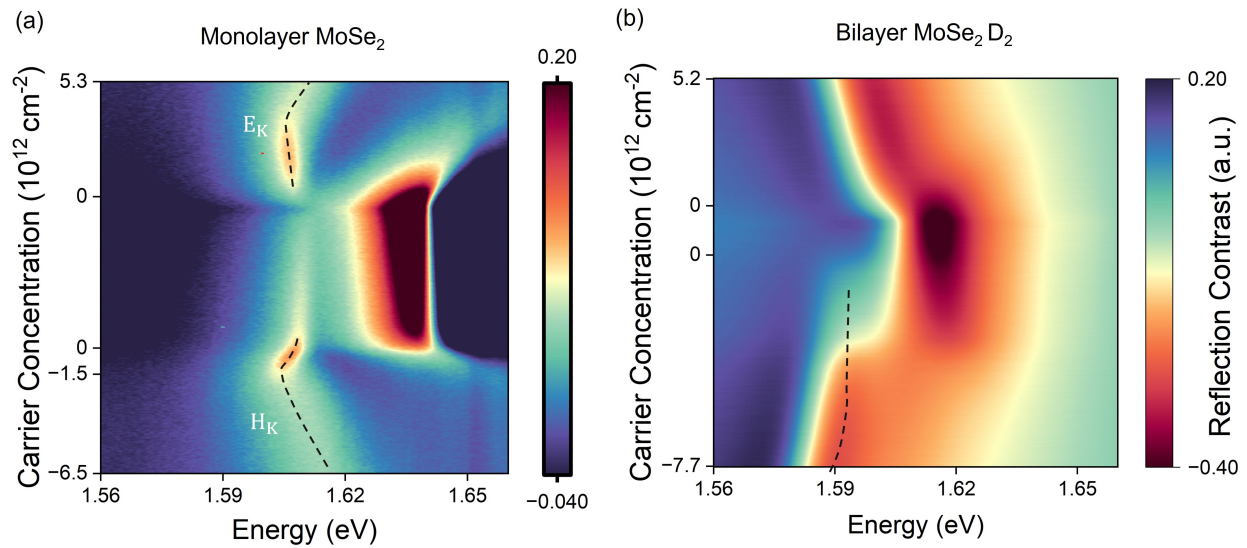
Extended Data Fig. 2: Doping dependent reflectivity spectra for the 59.6° reconstructed bilayer. (a) Picture of the sample. The white dashed line shows the twisted bilayer region. The scale bar is 10 μm . (b) Low frequency Raman spectrum of 59.6° sample. Only the shear mode is visible. (c) Differential reflectivity spectra of 59.6° sample. Only one positive trion H_1 is observed as doped holes are introduced, marked with a blue dashed line.



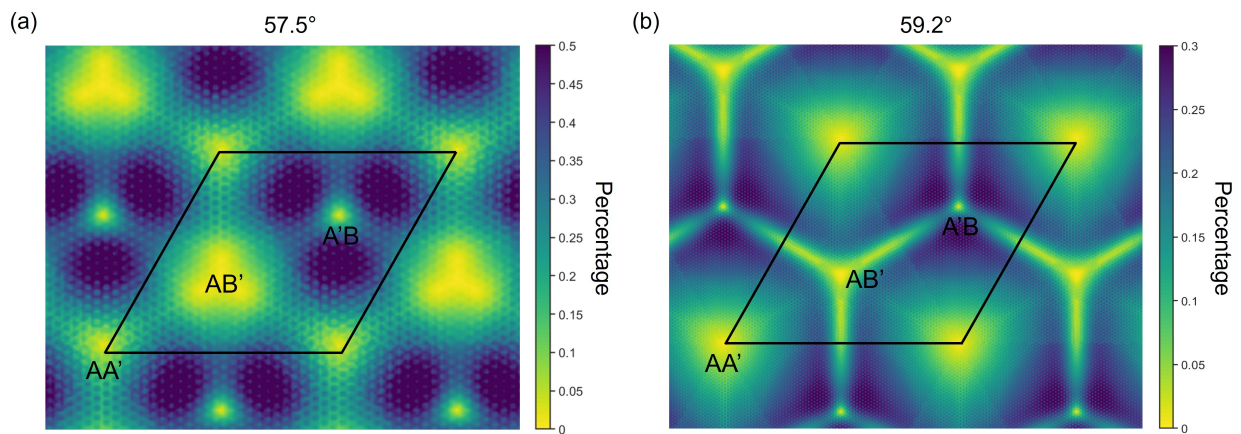
Extended Data Fig. 3: Lorentz fitting results of the 57.5° twisted bilayer device at selected doping levels (a-c). Red (green) curve corresponds to H_1 (H_2) and the blue curve corresponds to A exciton.



Extended Data Fig. 4: Doping dependent helicity-resolved reflectivity spectra. (a) The reflectivity spectra of the 57.5° twisted bilayer sample from a hole doping of $-1.4 \times 10^{13} \text{ cm}^{-2}$ to electron doping at $8.8 \times 10^{12} \text{ cm}^{-2}$. (b) Fitting results of helicity-resolved reflectivity spectra for 57.5° sample under a 2.5 T magnetic field. The circles show the fitted peak positions for H_1 and H_2 in different doping levels. The minimal difference between left and right polarizations indicates that the doped holes are located at the Γ valley. Both resonances are nearly constant below $-5 \times 10^{12} \text{ cm}^{-2}$.



Extended Data Fig. 5: Doping dependence reflection for the monolayer MoSe_2 and natural bilayer device D_2 . (a) Doping-dependent reflectivity for monolayer MoSe_2 . The dashed line represents the trion formed by dopants and electron-hole pairs at the K valley. (b) Reflectivity spectra from another natural bilayer device D_2 . The dashed line shows H_1 .



Extended Data Fig. 6: Lattice reconstructions in twisted bilayer MoSe_2 at (a) 57.5° and (b) 59.2° twist angle. The lattice reconstructions are defined as the local atomic displacements after relaxation.